Scanning Microscopy Vol. 12, No. 1, 1998 (Pages 71-80) 0891-7035/98$5.00+.25
Scanning Microscopy International, Chicago (AMF O'Hare), IL 60666 USA

SCANNING PROBE MICROSCOPY STUDIES OF ELECTRICALLY ACTIVE DEFECTS IN LATTICE MISMATCHED FILMS

Julia W.P. Hsu*, M.H. Gray and Q. Xu

Department of Physics, University of Virginia, Charlottesville, VA 22901

(Received for publication May 13, 1996 and in revised form September 3, 1996)

Abstract

We use a near-field scanning optical microscope (NSOM) to perform local photo-current measurements on strain-relaxed GeSi films on Si substrates. Topographic features and electrical activities of near surface defects are imaged simultaneously, allowing comparison among different sources of near-field photocurrent (NPC) contrast. We have achieved spatial resolution better than 100 nm in the NPC images, and can differentiate between surface and sub-surface defects. The resolution in NSOM photoresponse images is also examined through a two-dimensional calculation. We find that carrier diffusion length does not limit the resolution as previously thought. The ultra-high resolution achieved in NSOM is due to reduction of the excitation volume and of the carrier lifetime near defects.

Key Words: Near-field scanning optical microscopy, photocurrent, heteroepitaxy.

*Address for correspondence:
Julia Hsu
Department of Physics,
University of Virginia,
Charlottesville, VA 22901.
Telephone number: (804) 924-7956
FAX number: (804) 924-4576
E-mail: jhsu@virginia.EDU

Introduction

With advances in optoelectronics, e.g., the use of quantum well structures in lasers and photodetectors, the need to better characterize these submicron devices individually and to study single crystallographic defects is ever greater. While optical microscopes are the most valuable instruments in science laboratories, the diffraction-limited resolution of far field optics has prevented us from probing optical and optoelectronic properties of materials and devices on nanometer scale. The recent invention of the near-field scanning optical microscope (NSOM) (Pohl *et al*., 1984; Betzig *et al*., 1991) has made it practical to embark on such studies. Towards this end, NSOM has been used to investigate quantum well lasers (Buratto *et al*., 1994a; Goldberg *et al*., 1995), to probe local carrier dynamics (LaRosa *et al*., 1995), and to image *p-n* junctions (Buratto *et al*., 1994b; Goldberg *et al*., 1995; Unlu *et al*., 1995) and individual electrically-active defects (Hsu *et al*., 1994, 1996).

Because the sizes of individual crystalline defects are much smaller than the diffraction limit of visible light, defect characterization has been limited until now to electron microscopy techniques (Fitzgerald, 1991). The power of NSOM in defect imaging has been demonstrated (Hsu *et al*., 1994, 1996) to achieve a ten-fold increase in spatial resolution from far-field scanning optical microscopy (Wilson *et al*., 1979). Using the NSOM aperture as a localized light source, we performed photocurrent/photovoltage measurements to study threading dislocation defects on strain relaxed GeSi films with resolution comparable to what was obtained via electron beam-induced current (EBIC) (Leamy, 1982). While scanning force microscopy (SFM) has sub-angstrom sensitivity in detecting topographic changes and EBIC yields a direct image of local electrical properties, NSOM uniquely provides the capability to simultaneously study surface morphology and photo-response of the same defect structure non-destructively. In this paper, we apply the advantage of this correlation to differentiate among different types of defects. We also study the dependence of near-field photocurrent (NPC) contrast on the sample bias and the excitation modulation frequency. The empirical observations are compared with a simple, analytical model to understand NSOM resolution in NPC imaging of electrically active defects.

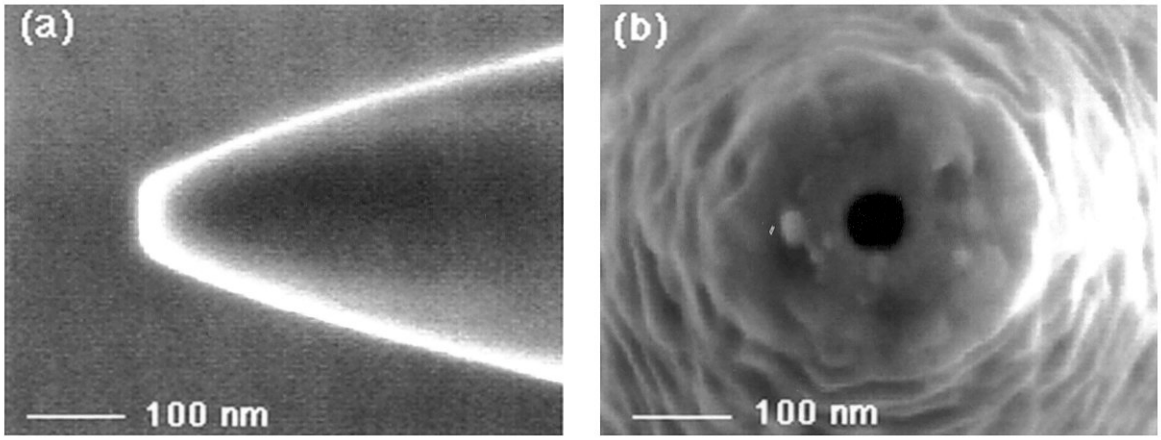

Figure 1: Field-emission SEM images of tapered fiber-optical NSOM tips. (**a**) The very end of tapered fiber without Al coating. The light outline of the tip is due to charging effect. (**b**) Head-on view of the same tip after ~ 135 nm of Al coating. The dark circle is the glass aperture, which is not obstructed by the Al coating. The size of the flat end of the uncoated tip and that of the aperture of the coated tip agree very well, ~ 60 nm.

Materials and Methods

Relaxed GeSi films are used to fabricate Si (Ge) heterojunctions with high two dimensional electron (hole) gas mobility (Mii *et al*., 1991; Schaffler *et al*., 1992; Xie *et al*., 1993) and to integrate GaAs and InGaP light emitting diodes on Si (Fitzgerald *et al*., 1992). Thus, the growth of good quality films having bulk properties on lattice mismatched substrates and the characterization of such films has been a major area of study in materials science. The strained-relaxed GeSi samples were grown on (001) Si substrates by molecular beam epitaxy at temperatures ~800 to 900°C. Their growth details and physical properties were reported by Fitzgerald *et al*. (1991, 1992) and Xie *et al*. (1992). The structure consists of a uniform Ge_xSi_{1-x} cap layer of ~1 μm on top of a compositionally graded layer on a 100 nm Si buffer layer. The grading rate was varied, but kept below 35% Ge/μm. The films are completely strain-relaxed, exhibiting bulk Ge_xSi_{1-x} optical properties (Fitzgerald *et al*., 1991; Xie *et al*., 1992). The samples have been extensively characterized (Fitzgerald *et al*., 1991, 1992; Hsu *et al*., 1992; Xie *et al*., 1992) by X-ray, Rutherford backscattering, electron microscopy and SFM to determine the degree of relaxation, composition, misfit dislocation network structure, threading dislocation densities, and surface roughness. Since the threading dislocations are carrier recombination centers, they are detrimental to any optoelectronic devices fabricated on these samples. Therefore, their density is kept as low as possible. Typically, these graded films have threading dislocation densities $\leq 5 \times 10^6$ cm^{-2}. This was determined with EBIC (Fitzgerald *et al*., 1992) because the density is too low to be detected by transmission electron microscopy (TEM).

Far-field optical microscopy has limited applications in defect imaging because crystalline defects are typically smaller than the diffraction limit of visible light. Since diffraction is a far-field phenomenon, optical resolution can be greatly improved by operating in the near-field regime. The ultrahigh resolution in near-field imaging arises because the evanescent modes have large wave-vector components parallel to the sample surface. Since these waves are non-propagating, the sample must be placed near the sub-wavelength aperture. The spatial extent of these evanescent waves is approximately the aperture size, a; thus, the resolution of a NSOM is $a << \lambda$, higher than the diffraction limit. The use of finely tapered, metal-coated optical fibers as sub-wavelength apertures led to a record 12 nm resolution with 514 nm light (Betzig and Trautman, 1992). The NSOM used in this experiment is modified from a PSI (Park Scientific Instruments) BD-2 scanning force microscope (PSI, Sunnyvale, CA). Instead of the silicon nitride cantilevers used in SFM, we used metal-coated, tapered optical fibers as NSOM tips. A shear force feed-back is added to regulate tip-sample separation. We use the feed-back circuit supplied with the SFM control electronics, but modify the feedback loop gain to achieve optimal performance for shear force. Data acquisition synchronized to scanning is performed using the SFM control electronics and software with simultaneous acquisition on two signal channels.

The NSOM tips are tapered, single mode optical fibers made by pulling while heating the fibers with a CO_2 laser. By controlling the laser power and spot size as well as the pulling force, we can vary the fiber tip diameters from ≤ 50 nm to ≥ 200 nm, as measured by a scanning electron microscope (SEM). The sub-wavelength apertures are defined by coating the

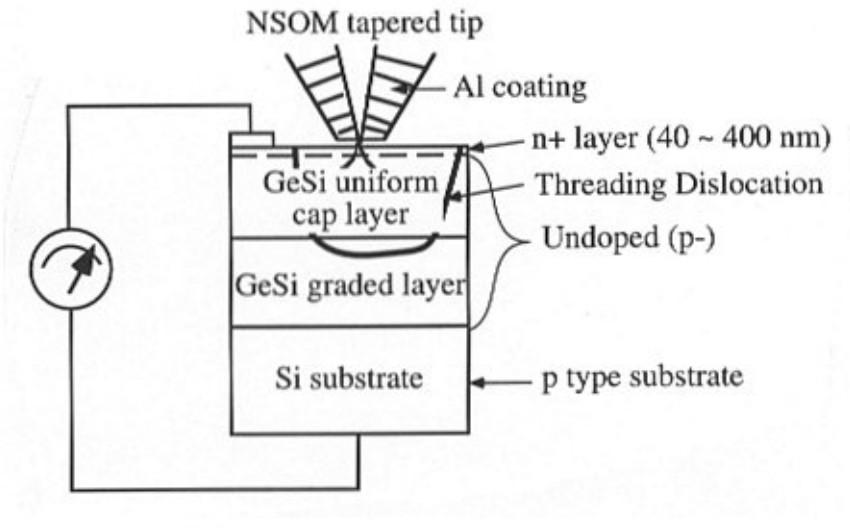

Figure 2: Schematic of NPC experiment on n+/i/p struc-ture. The carriers are photo-excited locally by the NSOM light and collected by the built-in *p-i-n* junction in the sample. The NPC image is created as the tip moves with respect to the sample.

sides of the tapered fiber with Al of thickness ≥ 100 nm. Figure 1a shows an SEM image of a tapered, uncoated fiber tip. The same tip with Al coating was imaged head-on and shown in Figure 1b. The glass aperture and the Al coating are clearly seen in the SEM image. The Al grains and roughness are also evident. For the tip shown on Figure 1, the aperture size is about 60 nm; Al coating did not obstruct the aperture. The NSOM light source is obtained by coupling laser light into the cleaved, untapered end of the fiber tips. All coated tips are inspected under a high power optical microscope for light leakage through pinholes. Only tips without pinholes are used for the experiment. The typical tips used in the experiment had ~150 nm apertures and optical output of ~50 nW with input power of ~1 mW.

In the near-field experiment, it is critical to regulate the tip-sample separation to prevent damaging the sample and/or the tip and to interpret the NSOM results correctly. Our NSOM setup includes a non-optical feed-back mechanism based on detecting shear force changes arising from tip-sample interaction at nanometer separation. The fiber tip is attached to a small piezo tube in order to dither the tip parallel to the sample surface at the resonance of the tip. The dithering is achieved by applying a small ac voltage (≤ 50 mV) to the piezo. The resonant frequencies of our tips with ~2 mm free length are typically 50 to 100 kHz. Due to the tip-sample interaction, the dithering amplitude at a fixed frequency and a fixed drive voltage decreases as the tip approaches the sample. The tip-sample interaction was measured by detecting changes in the electrical impedance of the dither piezo, and the tip-sample separation was regulated using a signal derived from this impedance change (Hsu *et al*., 1995; Lee *et al*., 1996). Compared to previous measurements where optical shear force feedback was used, the non-optical method significantly improves the NPC signal-to-noise ratio and increases the ease of the operation.

In this experiment, we photo-excite the GeSi samples with light from the NSOM tips and measure the spatial variation of the photoresponse as the sample is scanned beneath the tip. The laser source was a diode laser of 670 nm wavelength. Its intensity was electrically modulated before being coupled into the fiber tip. The modulation frequency can be varied from 1 kHz to 100 kHz. The samples have built-in *p-n* junctions parallel to the film surface (Fig. 2). Here, we report the study of two samples: sample #A has a *p+/n/n+* struc-ture and #B has a *n+/i/p* structure. Excess current due to the photo-excited carriers is detected using a current preamplifier. A dc voltage bias can be applied to the sample using the current preamp. The output voltage was demodulated using a lock-in amplifier before being sent to the computer. As the tip moves across the sample, topographic and NPC images were built up simultaneously. The topographic information was obtained automatically because we were regulating the tip-sample separation. The dependence of NPC on the sample bias and the excitation modulation frequency was examined. Images taken by detecting photovoltage changes are similar to those of photocurrent changes. The samples were not processed or etched prior to NSOM studies. Therefore, the topographic images reflect the as-grown surface morphology.

The small NSOM aperture limits the excitation volume and results in high spatial resolution. As the tip is brought into the near-field zone of the surface, the photocurrent signal increases by a factor of 2 to 3 due to the contribution of evanescent modes. Near electrically active defects, both traps and recombination centers, photoresponse should be lower than in defect-free regions. In these samples, the most prevalent electrically active defects are threading dislocations, which are expected to show up as dark spots in NPC images, similarly to those in EBIC images. By correlating the changes

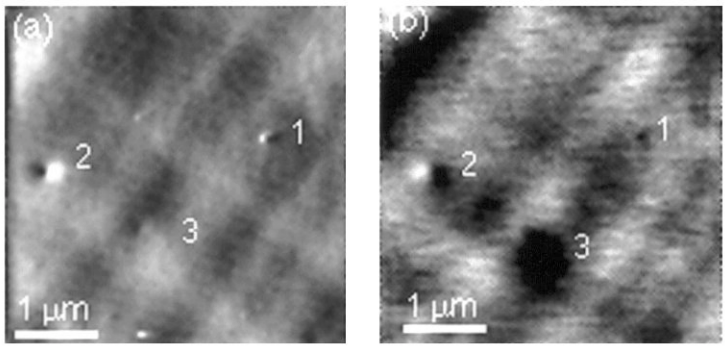

Figure 3: Simultaneously acquired (**a**) topographic and (**b**) NPC images of a relaxed GeSi film. The bars represent 1 μm. The grayscale in (**a**) represents 35 Å in height change and that in (**b**) represents 6% change in photocurrent. Cross-hatch patterns are evident in both images. Labels 1 to 3 represent three different types of sources responsible for point-like features in NPC images.

in the NPC im-ages with features in the topogra-phic images, we can learn about the electrical activities of near surface defects. In addition, we show that NSOM can reveal structures in recombination regions within individual defects.

NPC Results and Discussion

Figure 3 shows a typical NSOM image, displaying surface features and electrically active defects. The topographic image (Fig. 3a) shows that the surface morphology is dominated by the cross-hatch pattern that is characteristic of these compositionally graded, fully strain-relaxed GeSi films (Hsu *et al*., 1992). In the NPC image (Fig. 3b), the cross-hatch pattern shows a weak contrast which appears to be inversely correlated with the topography, i.e., the NPC signal is lower (higher) where the topography is higher (lower). Even more pronounced, the NPC image shows 3 dark spots. Spot #1 is due to a piece of debris on the surface, which shows up as a bump in the topographic image (Fig. 3a). Because the debris shadows the NSOM light from exciting carriers beneath it, it appears as a dark spot of equal dimensions to the topographic bump in the NPC image. Spot #2 displays a distinct and prominent surface pit in the topographic image; its photoresponse has an enhanced (bright) and a reduced (dark) region, i.e., a composition structure. The bright region to the right of the surface pit in the topographic image is due to a feedback circuit overshoot when a sudden topographic change is encountered. Although the feedback overshoot appears to be inversely correlated with the photoresponse, it is not the source for the NPC contrast, as will be shown explicitly in Figure 5. The composite structure of re-combination regions associated with these surface threading dislocations is characteristic of a sample, and is seen on some, but not all, samples. The sample studied in Figures 3 and 4 will be referred to as sample #A hence-forth. Spot #3 shows a larger, but non-distinct surface topographic feature, and a large, fuzzy NPC dark spot. We believe it is a sub-surface defect, in contrast to the surface defect exemplified by #2. These three are the most common features we observe on the relaxed GeSi samples. Surface defects of a different nature might have similar topographic features (Chen *et al*., 1995). Although, SFM has high sensitivity in detecting topographic changes, it cannot measure electrical properties. NSOM offers a unique capability to measure topographic changes and photoresponse at the same sample position with high sensitivities in both measurements, and therefore enables us to differentiate among different sources responsible for photocurrent variations.

The resolving power of NSOM in NPC images is demonstrated in Figure 4. Figures 4a and 4b are topographic and NPC images of three close-by defects. At the center of Figure 4a, there is a surface pit (#1) which has a strong NPC contrast associated with it in Figure 4b. Similar to what is shown in Figure 3, the recombination region of this surface defect is not simply a reduction in photoresponse, but also includes an enhanced photoresponse region. The less distinct surface topographic feature (#2) almost directly below this defect is a sub-surface defect. Even though the separation between these defects #1 and #2 is only ~1.2 μm, NSOM is able to distinguish between them, both topographically and electrically. A smaller defect (#3) is seen to the upper left of the center defect in Figure 4a. It does have a NPC contrast associated with it, though much weaker, which displays the composite (bright and dark) NPC contrast of surface defects on this sample. Figures 4c and 4d are zoom-in images of a surface defect, showing the details of recombination structures within it. On the lower left part of the images, there is a piece of debris with a reduction in NPC signal clearly seen in Figure 4d. There is no enhanced NPC signal associated with the debris. The threading dislocation defect in the center of the image shows a bright region in the NPC image, which almost coincides with the surface topographic depression. The reduced photoresponse region is to the upper right of the bright spot where the topography is not changing. The full width half maximum/minimum (FWHM) of the NPC reduction (dark spot) is ~200 nm, much closer to the aperture size than the carrier diffusion length.

As mentioned above, the shear force feedback tends

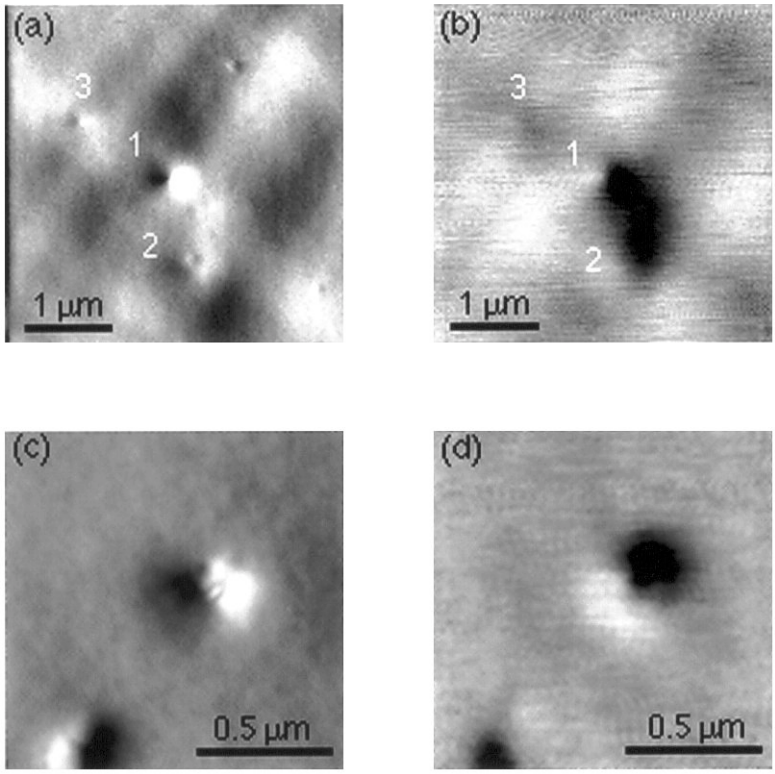

Figure 4: Simultaneously acquired (**a**) topographic and (**b**) NPC images of a relaxed GeSi film. The grayscale in (**a**) represents 35 Å height changes and that in (**b**) represents 12% change in photocurrent. (**c**) Topographic and (**d**) NPC images of another defect, showing the enhanced and reduced photocurrent regions associated with a single defect. The grayscale in (**c**) represents 50 Å height changes and that in (**d**) represents 12% change in photocurrent.

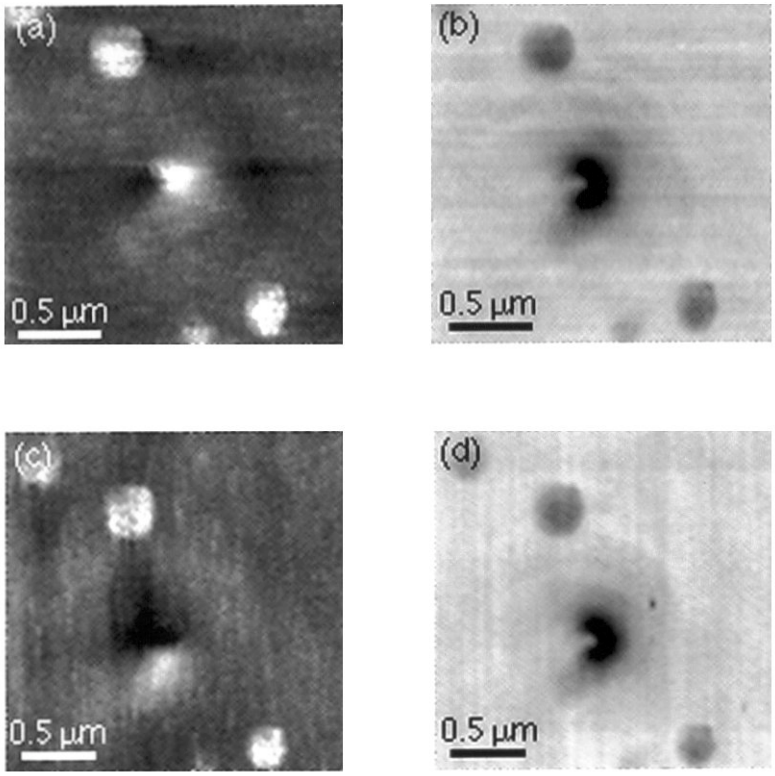

Figure 5: Images of a defect taken in orthogonal scan directions. (**a**, **c**) Topographic (grayscale = 65 Å) and (**b**, **d**) near-field photo-voltage images (grayscale = 10% signal change). The scan direction is from left to right in (**a**, **b**), and from top to bottom in (**c**, **d**). The feedback overshoots are evident as the bright spot to the right of the pit in (**a**) and that below the pit in (**c**).

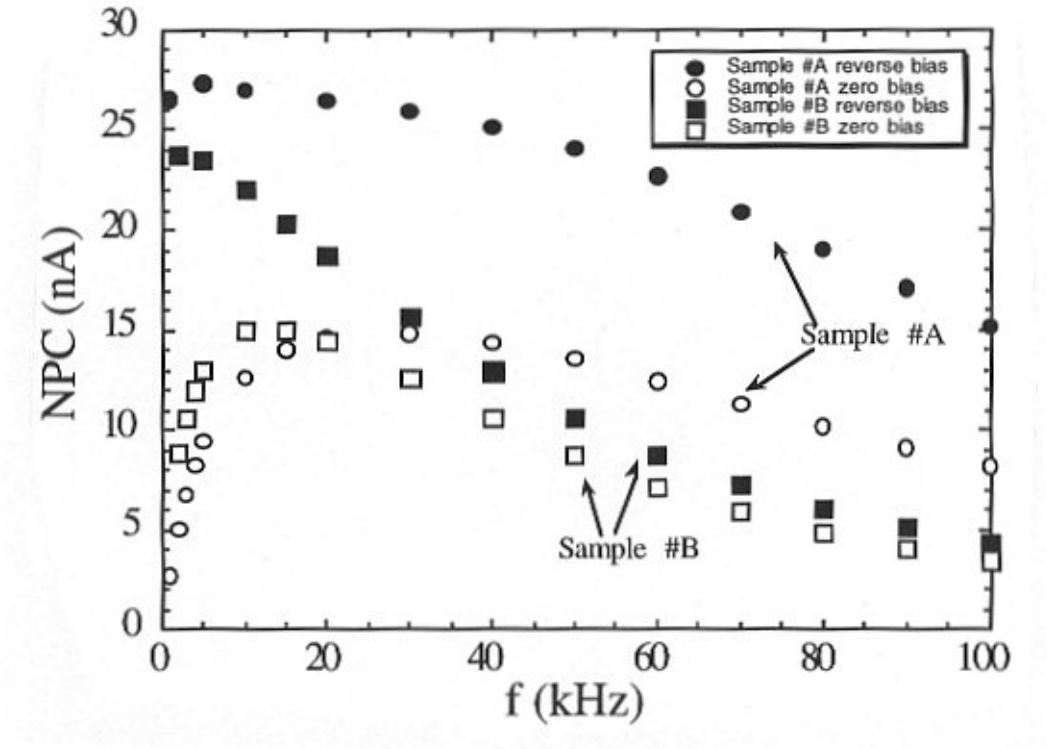

Figure 6: Frequency dependence of NPC signal. Circles represent data taken on sample #1 and squares represent sample #2. Solid symbols are for reverse bias (see text) and open symbols are for zero bias.

to overcompensate when sudden topographic changes are encountered. Since the evanescent modes exist near the aperture only, one might be concerned that a distance regulation error could cause erroneous NPC contrast. To address this concern, we have imaged the same defects with a 90° rotation in the scan direction. The results are shown in Figure 5. Figure 5a shows a threading dislocation pit in the center of the image and a debris to its upper left and two towards its lower right. The near-field photovoltage contrast in Figure 5b shows dark spots of the same dimensions as the debris, but the recombination region associated with the threading dislocation displays an asymmetric structure. Since the scan direction is horizontal and from left to right in Figure 5a, there is a bright spot to the right of the surface pit. To deconvolve the topographic effect, we imaged the same defects with the scan direction rotated 90° clockwise. Figures 5c and 5d show images taken with the scan direction vertical from top to bottom. Therefore, the feedback overshoot results in a bright spot below the pit in Figure 5c. As is clearly seen from Figure 5d, the region of reduced photovoltage signal has the same shape and same relationship with respect to the topographic pit as in Figure 5b. Therefore, the photoresponse contrasts associated with defects are unaffected by the scan direction and feedback overshoots. We believe the composite NPC contrasts observed above reflect structures of recombination regions within a defect, and are not an artifact of feedback errors.

Voltage bias applied to *p-n* junctions changes the depletion region width, and therefore the junction depth. EBIC measurements (Grillot *et al*., 1995) found dramatic differences in resolution and contrast between images taken under different bias conditions. The changes for different defects provide information on their depth-dependent recombination activities. Following the EBIC study, we performed NPC studies under different bias conditions. Reverse bias increases the photocurrent signal (Fig. 6) and, in most cases, enhances the signal-to-noise ratio in the NPC images. Forward bias has the opposite effect. Figures 3, 4 and 5 were taken under optimal reverse bias conditions: -1.0 V and +0.9 V to the top contract for sample #A and #B, respectively. However, there is little bias effect in the NPC image resolution or contrast. The weak bias dependence in the NPC images is intrinsic to near-field photoresponse. Since the evanescent modes only exist within approximately *a* from the sub-wavelength aperture, the near-

field experiment is much more surface sensitive than EBIC. Only defects near the surface can be resolved with submicron resolution. Sub-surface defects appear larger and fuzzier because the excitation spot size is larger at the depth of recombination activities (Hsu *et al*., 1996). Defects located deep beneath the surface will contribute only to background signal but will not appear as well-defined NPC features. To confirm the surface sensitivity of NSOM, we also performed NPC experiment by scanning over the same defect but with the tip ~ λ away from the surface. The resulting NPC image shows a gradual variation in signal, but does not show any submicron contrast associated with the defect. Therefore, all defects shown above, including the sub-surface defects, have depths of recombination activities < λ from the surface. Unlike EBIC, we cannot determine the depth of recombination activities by varying bias. In NPC imaging, it is the correlation between surface topographic features and the size of the photoresponse that differentiate between surface and sub-surface defects.

Varying the modulation frequency of the laser intensity provides a means to probe the carrier dynamics in the sample. Modulation frequency dependence of infrared transmission was shown to be related to local carrier lifetime (LaRosa *et al*., 1995). Figure 6 shows the frequency dependence of the photocurrent signal for two samples. All data were taken with the tip on the surface, i.e., feedback active. Open symbols represent data taken at zero bias and solid symbols represent data taken with reverse bias (-1.0 V and +0.9 V to the top contract for sample #A and #B, respectively). The NPC signal decreases at high frequencies for both samples, regardless of bias, although the frequency dependence is different between them. Unlike the infrared experiment, NPC measurements require making electrical contacts to the sample. Currently, we do not know whether this frequency dependence of the NPC signal is due to carrier life-time or contact capacitance. The striking feature in Figure 6 is the bias dependence at low frequencies. In the case of zero bias, the NPC signal increases below a certain frequency while under reverse bias, the NPC signal is only weakly dependent on frequency at low frequencies. We also measured the frequency dependence of the laser intensity modulation depth and found that it varies < 6% between 1 and 100 kHz. Therefore, the observed frequency dependence of the signal magnitude is a sample property, not a systematic error. In addition, frequency dependence of the NPC signal with the tip placed on the defect and on a defect-free region is the same. Despite the signal magnitude variation, NPC images taken with different modulation frequencies show little difference in contrast and resolution. We plan to make better contacts to minimize contact resistance/capacitance that might obscure the high frequency results. We also will test more samples to study the origin of low frequency bias dependence.

Two-Dimensional Analytical Model

Theoretical modeling is important for understanding resolution issues in near-field optical experiments. The resolution in NPC images, as well as in EBIC images, depends on the size of the carrier generation volume and the carrier diffusion length. While it is theoretically correct that diffusion length limits the resolution of EBIC and photoconductivity (Leamy, 1982; Wilson and Sheppard, 1984), it does not mean that two defects cannot be distinguished when the separation between them is smaller than the diffusion length. For real materials, defect separation is often larger than the size of the probe and smaller than the diffusion length. Hence, this is often the regime in which NSOM imaging operates. In such a case, how resolution should be defined is not clear.

In the NPC experiment, the steady-state carrier density is given by

$$\frac{\partial n(\vec{r})}{\partial t} = D\nabla^2 n(\vec{r}) - \frac{n(\vec{r})}{\tau(\vec{r})} + S(\vec{r}) = 0 \qquad (1)$$

where $n(\vec{r})$ is the carrier density, D is the diffusion constant, $\tau(\vec{r})$ is the carrier lifetime that has spatial dependence near defects, and $S(\vec{r})$ is a position-dependent source term due to the NSOM light. We recently solved eq. (1) in two dimensions (2D) both numerically (Xu Q, Gray MH, Hsu JWP, unpublished) and analytically with appropriate approximations. The analytical solution is summarized below. The NSOM light is taken to be a 2D delta function, $S(\vec{r}) = S_0 R^2 \delta(\vec{r} - \vec{r}_0)$, where R is the radius of the NSOM aperture and $\vec{r}_0$ is the position of the light source. The lifetime is assumed to change abruptly at the defect, i.e.,

$$\frac{1}{\tau(\vec{r})} = \frac{1}{\tau_0} + \frac{b^2}{\tau_1}\delta(\vec{r}) \qquad (2)$$

where the defect physical size is b and is located at the origin. The defect size is assumed to be smaller than R and diffusion lengths ($l_0 = \sqrt{D\tau_0}$ and $l_1 = \sqrt{D\tau_1}$). Since photocurrent experiment measures total carriers collected and not carrier densities, we must integrate $n(\vec{r},\vec{r}_0)$ to obtain $N(\vec{r}_0)$, the total carriers generated when the NSOM probe is located at $\vec{r}_0$. An image analogous to the NPC image is formed by plotting N as the probe is moved with respect to the defect.

The result for $N(x,y)$ near two close-by defects is shown in Figure 7. The full grayscale represents 10% change. The defects are modeled as two delta functions with radii b = 10 nm and separated by 0.5 μm. The radius of the photoexcitation (NSOM light) is assumed to be 50 nm and the intensity is taken to be 1 nW. We used 32 μm as the diffusion length (lifetime = 1 μs and diffusion constant = 10 cm^2/s) in the defect-

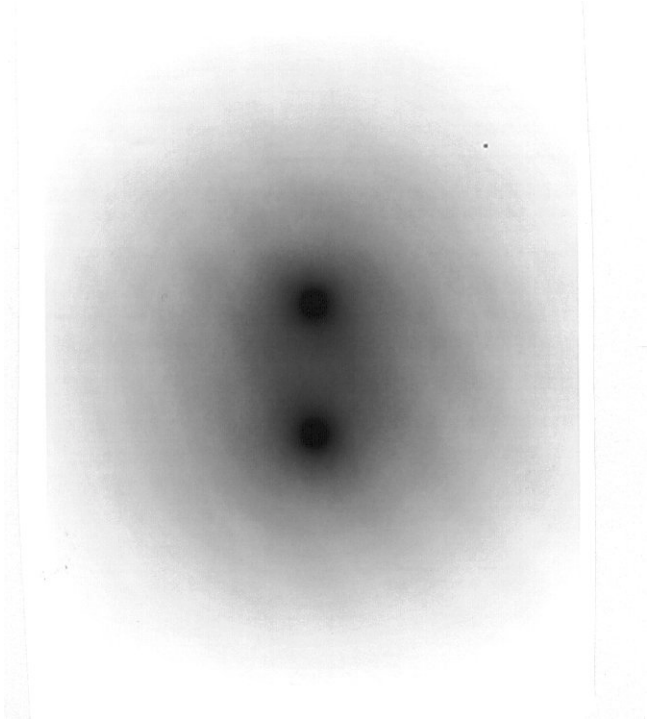

Figure 7: Calculated steady state carrier distribution (see text) near two defects 0.5 μm apart.

free region and 32 nm within the defects. It is clear from Figure 7 that the two defects are well resolved even though the bulk diffusion length is orders of magnitude larger. Varying the carrier lifetime in the defect-free region changes the overall signal but has small effect on the contrast. Increasing the carrier lifetime within the defects, however, dramatically reduces the defect contrast. Numerical studies, which will be published elsewhere, allow us to relax the restriction on defect size being the smallest length scale in the problem and to explore the competitive effects arising from generation, recombination, and diffusion.

Conclusions

We used a NSOM to probe the electrical activities of near surface defects on relaxed GeSi films. The images are not formed by collecting light, but by performing photocurrent/ photovoltage measurements as the tip moves with respect to the sample. In this somewhat unusual mode of NSOM operation, the light from the sub-wavelength aperture excites carriers locally and the excess carriers are collected by the built-in *p-i-n* junc-tions in the samples. We can clearly observe features in the photoresponse images localized in regions ≤ 200 nm. Furthermore, we observed composite structures in the recombination region associated with individual defects. The advantages of NSOM over other more commonly used techniques come from the simultaneous measurements of topographic changes and optical properties. We show that NPC contrast due to debris, surface, and sub-surface defects can be clearly distinguished. 2D calculations show that resolution in NPC and EBIC is not limited by carrier diffusion length. The high resolution demonstrated in this paper arises from the small size of the NSOM aperture, hence restricted excitation volume.

Acknowledgments

We thank E.A. Fitzgerald, Y.H. Xie, and P.J. Silverman for the GeSi samples, and A.T. Dorsey for helpful discussions regarding the 2D calculation. This work is supported by funding from NSF and Jeffress Trust. J.W.P.H. acknowledges a Sloan Research Fellowship.

References

Betzig E, Trautman JK, Harris TD, Weiner JS, Kostelak RL (1991). Breaking the diffraction barrier: Optical microscopy on a nanometer scale. Science **251**, 1468-1470.

Betzig E, Trautman JK (1992). Near-field optics: Microscopy, spectroscopy, and surface modification beyond the diffraction limit. Science **257**, 189-195.

Buratto SK, Hsu JWP, Betzig E, Trautman JK, Bylsma RB, Bahr CC, Cardillo MJ (1994a). Imaging InGaAsP quantum-well lasers using near-field scanning optical microscopy. J Appl Phys **76**, 7720-7725.

Buratto SK, Hsu JWP, Betzig E, Trautman JK, Bylsma RB, Bahr CC, and Cardillo MJ (1994b). Near-field photoconductivity: Application to carrier transport in InGaAsP quantum well lasers. Appl Phys Lett **65**, 2654-2566.

Chen KM, Jesson DE, and Pennycook SJ (1995). Cuspidal pit formation during the growth of Si_xGe_{1-x} strained films. Appl Phys Lett **66**, 34-36.

Fitzgerald EA (1991). Dislocations in strained-layer epitaxy: Theory, experiment, and applications. Mater Sci Rep (Netherlands) **7**, 87-142.

Fitzgerald EA, Xie YH, Green ML, Brasen D, Kortan AR, Michel J, Mii YJ, and Weir BE (1991). Totally relaxed Ge_xSi_{1-x} layers with low threading dislocation densities grown on Si substrates. Appl Phys Lett **59**, 811-813.

Fitzgerald EA, Xie YH, Monroe D, Silverman PJ, Kuo JM, Kortan AR, Thiel FA, Weir BE (1992). Relaxed Ge_xSi_{1-x} structures for III-V integration with Si and high mobility two-dimensional electron gases in Si. J Vac Sci Technol B **10**, 1807-1819.

Goldberg BB, Unlu MS, Herzog WD, Ghaemi HF, Towe E (1995). Near-field optical studies of semiconductor

heterostructures and laser diodes. IEEE J Sel Topics Quantum Electron **1**, 1073-1081.

Grillot PN, Ringel SA, Fitzgerald EA, Watson GP, Xie YH (1995). Minority- and majority-carrier trapping in strain-relaxed $Ge_{0.3}Si_{0.7}$/Si heterostructure diodes grown by rapid thermal chemical-vapor deposition. Appl Phys Lett **77**, 676-685.

Hsu JWP, Fitzgerald EA, Xie YH, Silverman PJ, Cardillo MJ (1992). Surface morphology of relaxed Ge_xSi_{1-x} films. Appl Phys Lett **61**, 1293-1295.

Hsu JWP, Fitzgerald EA, Xie YH, Silverman PJ (1994). Near-field scanning optical microscopy imaging of individual threading dislocations on relaxed Ge_xSi_{1-x} films. Appl Phys Lett **65**, 344-346.

Hsu JWP, Lee M, Deaver BS (1995). A non-optical tip-sample distance control method for near-field scanning optical microscopy using impedance changes in an electromechanical system. Rev Sci Instrum **66**, 3177-3181.

Hsu JWP, Fitzgerald EA, Xie YH, Silverman PJ (1996). Studies of electrically active defects in relaxed GeSi films using a near-field scanning optical microscope. J Appl Phys **79**, 7743-7750.

LaRosa A, Jahncke CL, Hallen HD (1995). Time as a contrast mechanism in near-field imaging. Ultra-microscopy **57**, 303-308.

Leamy HJ (1982). Charge collection scanning electron microscopy. J Appl Phys **53**, R51-R80.

Lee M, McDaniel EB, Hsu JWP (1996). An impedance based non-contact feedback control system for scanning probe microscopes. Rev Sci Instrum **67**, 1468-1471.

Mii YJ, Xie YH, Fitzgerald EA, Monroe D, Thiel FA, Weir BE, Feldman LC (1991). Extremely high electron mobility in Si/Ge_xSi_{1-x} structures grown by molecular beam epitaxy. Appl Phys Lett **59**, 1611-1613.

Schaffler F, Tobben D, Herzog HJ, Albstreiter G, Hollander B (1992). High-electron-mobility Si/SiGe heterostructures: Influence of the relaxed SiGe buffer layer. Semicond Sci Technol **7**, 260-266.

Pohl DW, Denk W, Lanz M (1984). Optical-stethoscopy: Image recording with resolution l/20. Appl Phys Lett **44**, 651-653.

Unlu MS, Goldberg BB, Herzog WE, Zun D, Towe E (1995). Near-field optical beam induced current measurements on heterostructures. Appl Phys Lett **67**, 1862-1864.

Wilson T, Osicki WR, Gannaway JN, Booker GR (1979). Comparison of dislocation images obtained using the scanning optical microscope and scanning electron microscope. J Mat Sci **14**, 961-965.

Wilson T, Sheppard CJ (1984). Theory and Practice of Scanning Optical Microscopy. Academic Press, New York. pp. 179-190.

Xie YH, Fitzgerald EA, Silverman PJ, Kortan AR, Weir BE (1992). Fabrication of relaxed GeSi buffer layers on Si(100) with low threading dislocation density. Mat Sci Eng B **14**, 332-335.

Xie YH, Monroe D, Fitzgerald EA, Silverman PJ, Thiel FA, Watson GP (1993). Very high mobility two-dimensional hole gas in Si/Ge_xSi_{1-x}/Ge structures grown by molecular beam epitaxy. Appl Phys Lett **63**, 2263-2264.

Discussion with Reviewers

M.S. Unlu: Authors suggest that the near-field photocurrent data displaying FWHM in the order of 200 nm indicate that the diffusion length does not limit the resolution. The samples used in this study have a *p-n* junction very close to the surface. Therefore, the photogenerated carriers are collected by the built-in field at the *p-n* junction before they can diffuse in the lateral dimension and be captured by nearby defects. The presence of this boundary with the underneath depletion region effectively reduces the diffusion length to approximately the thickness of the top n+ layer. For thick (or bulk) epilayers, the diffusion length of the photogenerated carriers will remain as a limitation on the resolution for excitation mode NSOM.

Authors: We agree with the referee that the *p-n* junction has an important effect, but we disagree with him on that the diffusion length is reduced to the thickness of the top n+ layer. The most important consequence of using *p-n* junctions to collect carriers is that we can separate carrier motion in the plane of sample surface (x-y) from that perpendicular to the surface (z). In the z direction, the carrier transport is predominantly drift because of the built in electric field, while diffusion dominates carrier spread in the x-y plane. Therefore, we can treat carrier distribution in the x-y plane, which determines the resolution in NPC imaging, with a two-dimensional diffusion model. As we showed in this paper, two nearby defects are clearly resolved (Fig. 7) even though their separation distance is much shorter than the diffusion length.

As for the drift in the z direction, our samples have *p-i-n* structures, not *p-n* structures. The depletion region in the samples is about the same as the thickness of the film, ~ 4 μm. As the carriers, which are generated by a point source, travels towards the contacts in the z direction in the depletion region, they can spread laterally in the x-y plane. It is true that carriers do not recombine in the depletion region, but they do diffuse. Therefore, the "effective diffusion length" for our samples should be $\sqrt{Dt_{dr}}$, where t_{dr} is the drift time across the depletion layer. This point has been discussed in our previous paper (Hsu *et al*., 1996). The "effective diffusion length" is not the top n+ layer thickness because the n+ layer is so heavily doped that the minority life-time is extremely short there.

The high resolution we obtained in the NPC images is the result of small excitation volume and the reduced carrier lifetime near dislocation defects. For thick epilayers, the total photocurrent will be reduced, but the resolution of defect

imaging will not be limited by diffusion given high enough signal to noise ratio.

C.K. Shih: As mentioned by these authors, EBIC is another technique which allows one to probe the local electrical characteristics of defects. It is, therefore, important to compare these two techniques. What are the potential applications that this technique possesses that cannot be achieved by using EBIC? If any, elaborate a little bit. Otherwise, why should one use NPC since EBIC can be tuned to provide depth information?
Authors: As we show in this paper, we have achieved higher resolution than EBIC with near-field photocurrent imaging. In addition, there is no charging effect in our measurement. Most importantly, it is easier to model and obtain quantitative results (see below) with NPC data, as we begin to do in this paper. Due to the "ballooning" effect of electron beam in materials, quantitative analysis of EBIC is more difficult. However, the disadvantages of scanning probe microscopy are limited scan size and slow scan speed.

C.K Shih: The two-dimensional analytical model is aimed at addressing the resolution issues in the NPC. While not being able to analyze their analysis in details, I believe these authors have performed a fine job. The conclusion about the resolution is also convincing. I do have one question though: assuming that the diffusion coefficient of the free carrier is known, can this analytical model be refined to a point that one can analyze the NPC signal profile across the defect and estimate the carrier lifetime near a defect?
Authors: Yes. Given the average carrier lifetime in the defect-free region and the source size (from SEM images), we can fit the results of numerical calculations to experimental data and obtain carrier lifetime in the defect. We have done such analysis, which will be published in another paper.